# **DogMo:** A Large-Scale Multi-View RGB-D Dataset for 4D Canine Motion Recovery

Zan Wang<sup>1</sup>\*, Siyu Chen<sup>1</sup>\*, Luya Mo<sup>1</sup>\*, Xinfeng Gao<sup>1</sup>\* Yuxin Shen<sup>1</sup>, Lebin Ding<sup>1</sup>, Wei Liang<sup>1,4</sup>†

\* Equal contributors † Corresponding authors

https://pie-lab.cn/DogMo/



Figure 1: We present  $\textbf{\textit{DogMo}}$ , a large-scale multi-view RGB-D video dataset capturing diverse canine movements using 5 synchronized low-cost cameras.  $\textbf{\textit{DogMo}}$  contains 1.2k motion sequences from 10 unique dog instances, spanning 11 action types and totaling over 220 minutes of recordings.

#### Abstract

We present DogMo, a large-scale multi-view RGB-D video dataset capturing diverse canine movements for the task of motion recovery from images. DogMo comprises 1.2k motion sequences collected from 10 unique dogs, offering rich variation in both motion and breed. It addresses key limitations of existing dog motion datasets, including the lack of multi-view and real 3D data, as well as limited scale and diversity. Leveraging DogMo, we establish four motion recovery benchmark settings that support systematic evaluation across monocular and multi-view, RGB and RGB-D inputs. To facilitate accurate motion recovery, we further introduce a three-stage, instance-specific optimization pipeline that fits the SMAL model to the motion sequences. Our method progressively refines body shape and pose through coarse alignment, dense correspondence supervision, and temporal regularization. Our dataset and method provide a principled foundation for advancing research in dog motion recovery and open up new directions at the intersection of computer vision, computer graphics, and animal behavior modeling.

Preprint. Under review.

<sup>&</sup>lt;sup>1</sup> School of Computer Science & Technology, Beijing Institute of Technology

<sup>&</sup>lt;sup>2</sup> Yangtze Delta Region Academy of Beijing Institute of Technology, Jiaxing

## 1 Introduction

Over the past decade, human body recovery from images and videos has made remarkable progress, driven by the release of numerous large-scale public datasets [Mahmood et al., 2019; Black et al., 2023], standardized benchmarks [Ionescu et al., 2013; Von Marcard et al., 2018], and advanced algorithmic frameworks [Bogo et al., 2016; Kanazawa et al., 2018; Li et al., 2022; Shin et al., 2024]. As interest in animal welfare and the pet industry continues to grow, efforts have emerged to extend human motion recovery methods to animals [Zuffi et al., 2017; Biggs et al., 2020; Rüegg et al., 2022; Sabathier et al., 2024] for behavior analysis and virtual asset creation. However, progress in this area remains limited, primarily due to the lack of comprehensive animal datasets, which constrains advancements in algorithm design and evaluation.

Acquiring animal motion data is inherently inefficient and costly due to the lack of a tailored toolchain and the fact that animals, unlike humans, cannot follow instructions consistently during capture. Consequently, publicly available animal datasets are scarce and suffer from two major issues:

- Lack of multi-view and real 3D. Most datasets [Biggs et al., 2019; Yu et al., 2021; Yang et al., 2022b] consist of monocular RGB videos, lacking both multi-view recordings and accurate 3D information, which limits the study of multi-view settings and the recovery of real 3D shapes.
- Limited scale and diversity. Existing datasets [Kearney et al., 2020; Luo et al., 2022; Shooter et al., 2024a;b] typically contain less than one hour of footage, with minimal variation in motion types and animal instances.

In this work, we focus on motion recovery for dogs, one of the most common companion animals in human life. To address the aforementioned issues, we introduce  $\textbf{\textit{DogMo}}$ , a large-scale multi-view RGB-D video dataset capturing dog movements, collected using 5 low-cost RGB-D cameras that are carefully synchronized and calibrated, as illustrated in Fig. 1. These cameras are evenly distributed around a capture zone to record dog movements from multiple viewpoints. Within this zone, dogs are encouraged to perform natural behaviors such as running, jumping, and interacting with humans. In total,  $\textbf{\textit{DogMo}}$  collects 1.2k motion sequences from 10 unique dog instances, with a total duration exceeding 220 minutes. Built upon this dataset, we establish four canine motion recovery settings, *i.e.*, recovering 4D dog motions from (1) monocular RGB videos, (2) multi-view RGB videos, (3) monocular RGB-D videos, and (4) multi-view RGB-D videos.

Despite significant progress in human motion recovery, estimating dog motion from visual observations presents unique challenges. First, the wide variation in body size across breeds limits the model's generalization capability. Yet prior works [Zuffi et al., 2017; Biggs et al., 2020; Yang et al., 2023] primarily address monocular shape estimation, which inherently suffers from ambiguities in recovering absolute body shape. Second, dogs' fur-covered and often textureless appearance makes body parts visually indistinct, hindering accurate localization. Approaches such as Rüegg et al. [2022]; Sabathier et al. [2024] depend on pre-trained keypoint detectors or part segmentation models, but they overlook the potential of temporal motion priors to regularize parts and joints across time.

To address these challenges, we first extend D-SMAL [Zuffi et al., 2017; Rüegg et al., 2022] with an additional scaling factor to better deal with the broad variation in dog body shapes. Building on this extension, we propose a three-stage instance-specific optimization pipeline that fits the model parameters to input images in a coarse-to-fine manner. The first stage performs a lightweight coarse optimization to initialize the global translation, orientation, and body shape, substantially reducing the optimization space and improving overall efficiency. In the second stage, following Sabathier et al. [2024], we leverage Continuous Surface Embedding (CSE) [Neverova et al., 2020] for dense correspondence supervision, augmented with regularization terms to address the unique leg-crossing issue and to constrain shape and pose variations. Finally, the third stage refines the entire motion sequence with a temporal loss that enforces smoothness and mitigates local optima arising from noisy keypoint estimates in individual frames.

We summarize the contributions as: (1) We introduce **DogMo**, a large-scale multi-view RGB-D dataset for 4D dog motion recovery, addressing key limitations of existing datasets, including the lack of multi-view coverage and real 3D information, and sufficient data scale and diversity. (2) Based on **DogMo**, we establish four benchmark settings spanning monocular and multi-view, RGB and RGB-D inputs, aiming to facilitate further research in animal motion recovery and related downstream applications. (3) We propose a three-stage instance-specific optimization pipeline that progressively refines SMAL parameter estimation from coarse to fine.

## 2 Related Work

Model-Free 3D Animal Reconstruction Model-free 3D animal reconstruction from images or videos either employs instance-specific 3D shape optimization [Cashman and Fitzgibbon, 2012; Yang et al., 2021; Wu et al., 2022; Yang et al., 2023] or trains neural networks to directly regress 3D structures without requiring 3D supervision [Wu et al., 2023b; Liu et al., 2023b; Wu et al., 2023a; Yao et al., 2023a; Aygun and Mac Aodha, 2024; Li et al., 2024c]. Both approaches avoid reliance on parametric models and primarily leverage differentiable rendering to enforce 2D supervision, such as silhouettes, keypoints, and semantic correspondences. While the former is typically tailored to individual instances, the latter aims to generalize across diverse articulated animal species by learning from large-scale internet image collections. More recent efforts have shifted toward building neural implicit representations for animals [Luo et al., 2022; Yang et al., 2022a; Sinha et al., 2023; Tan et al., 2023; Tu et al., 2025; Yang et al., 2025], or distilling 3D reconstructions from 2D generative models [Ho et al., 2020; Rombach et al., 2022] by extending Score Distillation Sampling (SDS) [Poole et al., 2023] to image-conditioned multi-view generation models [Liu et al., 2023c; Qian et al., 2024; Shi et al., 2024]. Our focus is on model-based 4D dog motion recovery from a wide range of visual inputs, spanning monocular and multi-view, RGB and RGB-D inputs.

Model-Based Animal Pose and Shape Estimation 
Model-based animal pose estimation from 2D observations, such as 2D [Cao et al., 2019; Yu et al., 2021; Yang et al., 2022b; Zeng et al., 2024; Ye et al., 2024] and 3D [Kearney et al., 2020; Bala et al., 2020; Muramatsu et al., 2022; Sosa and Hogg, 2023; Shooter et al., 2024a] keypoint detection, plays a crucial role in animal behavior analysis. Leveraging parametric animal models like SMAL [Zuffi et al., 2017] and ABM [Badger et al., 2020], recent approaches aim to directly estimate pose and shape parameters from images, as these models provide strong priors over animal body shape and articulation. These methods typically either optimize [Zuffi et al., 2017; Wang et al., 2021; Li et al., 2021; Sabathier et al., 2024] or regress [Biggs et al., 2020; Li and Lee, 2021; Rüegg et al., 2022; 2023; Li et al., 2024b] the parameters from observations, often relying on 2D re-projection losses due to the absence of ground-truth 3D annotations. Some studies [Zuffi et al., 2019; Lyu et al., 2024; Shooter et al., 2024a] instead train models to directly regress 3D pose and shape using synthetic data or motion capture datasets, though these approaches are often limited in data diversity and scale. We propose a unified three-stage pipeline for progressively fitting the SMAL model to video sequences, demonstrating its robust performance across various visual inputs.

**Animal-Related Datasets** Early datasets for animal analysis mainly comprise 2D images or videos annotated with 2D labels, enabling tasks such as classification [Khosla et al., 2011], detection [Liu et al., 2023a], segmentation [Mu et al., 2020; Deane et al., 2024], 2D/3D pose estimation [Biggs et al., 2019; Cao et al., 2019; Biggs et al., 2020; Yu et al., 2021; Joska et al., 2021; Yang et al., 2022b; Yao et al., 2023b], and behavior understanding [Li et al., 2020; Ng et al., 2022; Ma et al., 2023]. Compared to these datasets, some works leverage simulators to synthesize animal images [Zuffi et al., 2019; Shooter et al., 2024a;b; Lyu et al., 2024], which provide access to 3D pose. Other efforts rely on expensive capture devices, such as motion capture systems or 3D scanners, to acquire high-quality 3D data of horses [Li et al., 2024a; Zuffi et al., 2024], birds [Naik et al., 2023], and rats [Marshall et al., 2021]. Kearney et al. [2020] collect RGB-D data of dogs using a Kinect V2 camera, supplemented with MoCap to obtain accurate 3D poses. Xu et al. [2023] generate pseudo ground-truth 3D annotations by manually fitting the SMAL model to 2D images. Rodent3D [Patel et al., 2023] provides multi-view, multi-modal video recordings of mice to facilitate pose tracking and behavioral analysis. The emergence of Neural Radiance Field (NeRF) has inspired datasets [Luo et al., 2022; Sinha et al., 2023] that leverage multi-view imaging or video to reconstruct detailed 3D neural animals. This work introduces a new large-scale multi-view RGB-D video dataset capturing diverse canine movements, aimed at facilitating research in dog motion recovery and related fields.

# 3 DogMo Dataset

#### 3.1 Data Capture

**Device Setup** We collect dog motion data using a low-cost capture system equipped with 5 ORBBEC Astra 2<sup>1</sup> RGB-D cameras. The cameras are evenly distributed along a circular area with a

ORBBEC Astra 2: https://www.orbbec.com/products/structured-light-camera/astra-2/

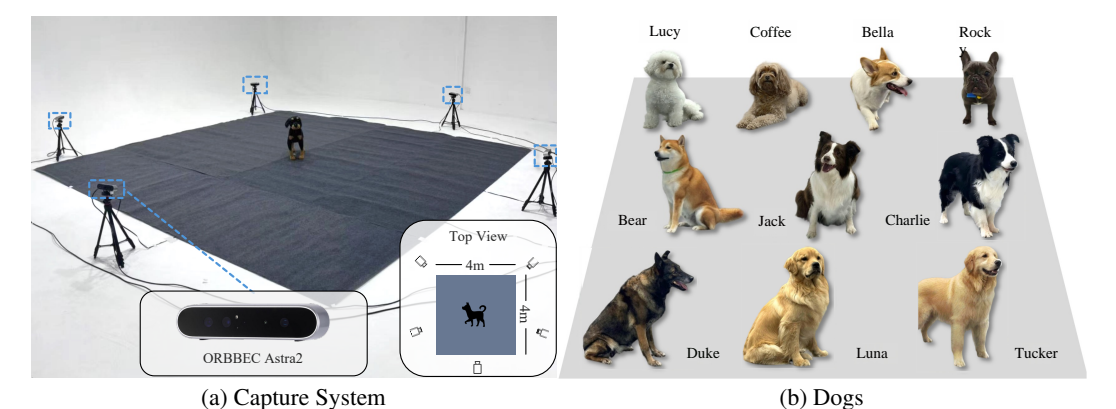


Figure 2: Motion Capture. We employ 5 synchronized low-cost RGB-D cameras to record 10 individual dogs.

radius of approximately 2.5 meters, all oriented toward the center of the capture zone. Each camera is positioned at a height of about 0.45 meters, with a random pitch angle within  $\pm 10$  degrees. Fig. 2 exhibits the overview of the capture setup.

For camera calibration, we leverage the OpenCV library [Bradski, 2000] to manually calibrate each pair of adjacent cameras, thus deriving the relative poses of any two cameras. To synchronize all cameras, we employ the Sync Hub Dev<sup>2</sup> device provided by ORBBEC.

**Capture Procedure** During data collection, a dog trainer guides the dog to perform specific actions within the capture zone by issuing semantic commands, such as running, jumping, or playing with humans. We ensure that the dog remains within the capture area so that at least three cameras can simultaneously capture the dog's full body. Since the trainer needs to actively guide the dog, occasional occlusions of the dog by the trainer are unavoidable from certain viewpoints.

#### 3.2 Dataset Statistics

In DogMo, each camera records synchronized RGB and depth streams, with RGB images at a resolution of  $1920 \times 1080$  and depth images at  $1600 \times 1200$ . The RGB and depth frames are hardware-aligned within the camera. The system operates at 15 FPS. DogMo contains 1.2k motion clips collected from 10 unique dog instances, as displayed in Fig. 2b. Each motion clip lasts between 0.87 and 19.07 seconds, covering 11 action types ranging from running to playing with humans. In total, the dataset provides over 220 minutes of motion footage, amounting to more than 1M frames across all camera views. To further support research, we annotate each frame with binary masks and keypoints of the dog, and assign a semantic label to each motion. We provide an overview of DogMo in Fig. 3, and a comparison with existing related datasets is summarized in Tab. 1.

Table 1: **Comparison between** *DogMo* **and existing related datasets.** The notation \* indicates that nearly all dog motions in the CoP3D dataset are in a sprawling posture throughout the entire video.

Dataset	Modality	FPS	Resolution	#Views	#Frames	#Subjects	#Actions	Sync. / Real
CoP3D [Sinha et al., 2023]	RGB	-	$720 \times 1280$	1	600k	4,200	1*	Real
Sydog-video [Shooter et al., 2024b]	RGB	25	$1024\times1024$	1	87.5k	5	5	Sync.
Digidogs [Shooter et al., 2024a]	RGB-D	-	$1280 \times 720$	1	27.9k	8	12	Sync.
RGBD-Dogs [Kearney et al., 2020]	RGB-D	6	$2560 \times 1440$	6	1.9k	7	5	Real
DogMo (Ours)	RGB-D	15	$1920\times1080$	5	1M	10	11	Real

# 4 Method

#### 4.1 Problem Formulation

Given a video sequence  $\{\mathbf{I}_t\}_{t=1}^T$ , our goal is to reconstruct the 3D posed mesh of a canine subject, parameterized by D-SMAL [Zuffi et al., 2017; Rüegg et al., 2023] parameters  $\{\mathbf{S}_t\}_{t=1}^T$ . Each frame  $\mathbf{I}_t$  can be a single-view RGB, multi-view RGB, single-view RGB-D, or multi-view RGB-D input, where T denotes the number of frames. For simplicity, we denote the RGB and depth images

 $<sup>^2</sup>$ Sync Solutions: https://www.orbbec.com/products/camera-accessories/sync-solutions/

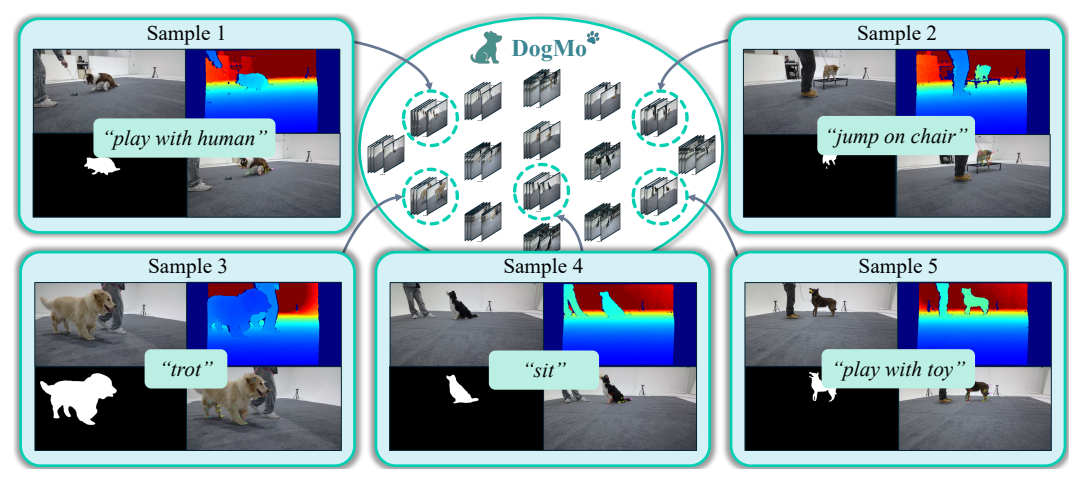


Figure 3: **Overview of** *DogMo. DogMo* provides five-view RGB-D image sequences for each motion recording, along with corresponding instance masks, keypoints, and semantic (*i.e.*, action label) annotations.

as  $C_t$  and  $D_t$ , respectively. The D-SMAL parameters at each frame are represented as a 5-tuple  $\mathbf{S}_t = (\beta, \theta_t, \gamma_t, \phi_t, s)$ , where  $\beta \in \mathbb{R}^{30}$  represents the shape parameters,  $\theta_t \in \mathbb{R}^{6N}$  denotes the N joint rotations in 6D representation,  $\gamma_t \in \mathbb{R}^3$  is the global translation, and  $\phi_t \in \mathbb{R}^6$  is the global orientation. To accommodate the broader range of dog sizes, we introduce s as an additional scaling parameter for resizing the body mesh, extending the original D-SMAL formulation. Given these parameters, the D-SMAL model finally outputs a posed 3D mesh, defined as

$$V, \mathcal{F} = \mathcal{M}(\beta, \theta, \phi) \times s + \gamma, \tag{1}$$

where  $\mathcal{V} \in \mathbb{R}^{3889 \times 3}$  are the mesh vertices,  $\mathcal{F} \in \mathbb{N}^{7774 \times 3}$  is a list of triangular faces, and  $\mathcal{M}(\cdot)$  is original skinning function of D-SMAL.

#### 4.2 Canine Motion Recovery

To encourage temporal smoothness of the results, we follow Sabathier et al. [2024] and model the time-varying tuple  $(\theta_t, \gamma_t, \phi_t)$  as the output of an multilayer perceptron (MLP) network conditioned on a smooth timestep embedding  $\tau(t)$ , instead of directly optimizing the D-SMAL parameters. Here,

$$\theta_t, \gamma_t, \phi_t = \text{MLP}_{\psi}(\tau(t)).$$
 (2)

In contrast, the body shape parameters  $\beta$  and the scaling factor s are treated as time-invariant and are directly optimized. During the optimization, we adopt a three-stage optimization pipeline that progressively recovers the MLP parameters  $\psi$ , body shape parameter  $\beta$ , and the scaling factor s, from coarse to fine, as detailed below. Fig. 4 presents the overview of the optimization pipeline.

# 4.2.1 Stage 1: Coarse Alignment.

In the first stage, we initialize the parameters  $(\gamma_t, \phi_t, s)$  by coarsely aligning the projected 3D model with the observed data. This alignment is guided by three frame-specific loss terms defined below.

**Chamfer Mask Loss** The Chamfer Mask Loss encourages alignment between the projected D-SMAL mesh and the observed dog silhouette, defined as:

$$\mathcal{L}_t^{\text{mask}} = \text{CD}\left(\left\{u \mid u \in C_t \odot M_t\right\}, \left\{\mathcal{R}(X) \mid X \in (\mathcal{V}_t, \mathcal{F}_t)\right\}\right). \tag{3}$$

Here, u denotes the 2D pixels occupied by the dog, derived from the segmentation mask  $M_t$ ; and  $M_t$  is predicted by the off-the-shelf Grounded SAM 2 [Ren et al., 2024] using the text prompt "dog."  $\mathcal{R}(\cdot)$  denotes the camera projection operation, which projects 3D points onto the 2D image plane using a fixed projection matrix shared across all frames under the assumption of a static camera setup. X represents 3D points sampled from the posed mesh  $(\mathcal{V}_t, \mathcal{F}_t)$ . To better capture leg motion, we increase the sampling density in regions corresponding to legs, improving their silhouette alignment.

**Sparse Keypoint Loss** To further enforce alignment between the keypoints of the 3D model and observed 2D keypoints, we apply the Sparse Keypoint Loss defined as:

$$\mathcal{L}_t^{\text{kp}} = \|h(C_t) - \mathcal{R}(\mathcal{J}_t)\|, \qquad (4)$$

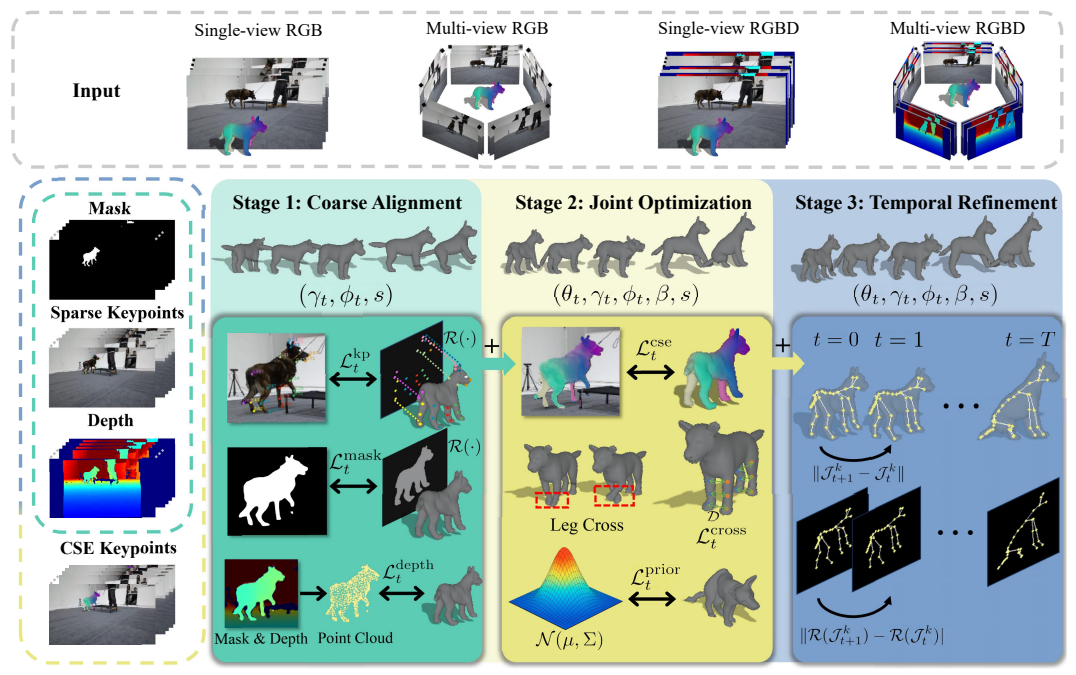


Figure 4: **Optimization pipeline.** Our optimization pipeline includes three stages, progressively refining the dog's body shape and pose through coarse alignment, dense correspondence supervision, and temporal regularization.

where  $h(C_t)$  denotes the 2D keypoints detected from the image  $C_t$  using the sparse dog keypoint detector from BARC [Rüegg et al., 2022], and  $\mathcal{R}(\mathcal{J}_t)$  represents the projection of the corresponding 3D keypoints  $\mathcal{J}_t$  from the estimated D-SMAL mesh.

**Chamfer Depth Loss** To exploit per-pixel depth supervision when depth input is available, we incorporate a Chamfer Depth Loss defined as:

$$\mathcal{L}_t^{\text{depth}} = \text{CD}(\{v \mid v \in \mathcal{R}^{-1}(M_t \odot D_t)\}, \{X \mid X \in (\mathcal{V}_t, \mathcal{F}_t)\}.$$
 (5)

Here,  $\mathcal{R}^{-1}$  denotes the inverse camera projection operation, which uses the depth map and the camera projection matrix to lift the masked depth image pixels into 3D space. This loss measures the Chamfer Distance between the resulting point cloud and the sampled points on the estimated dog mesh. We use this term in settings that include depth input.

## 4.2.2 Stage 2: Joint Optimization.

In the second stage, we optimize all parameters through a more comprehensive, frame-specific loss function, which includes three additional loss terms beyond the previously introduced terms.

**CSE Keypoint Loss** Following Sabathier et al. [2024], we incorporate a CSE Keypoint Loss to enforce denser correspondence supervision. This loss is defined as:

$$\mathcal{L}_{t}^{\text{cse}} = \sum_{u \in M_{t} \odot C_{t}} \|u - \mathcal{R}(\text{CSE}(\mathcal{V}, u))\|,$$
(6)

which penalizes the distance between each foreground pixel u in the dog mask and the 2D projection of its corresponding 3D point on the D-SMAL mesh. The correspondence is provided by the image-to-CSE predictor CSE( $\cdot$ ) [Neverova et al., 2020].

**Leg Cross Loss** To prevent unnatural intersections between the left and right legs of the posed D-SMAL model, we introduce a Leg Cross Loss defined as:

$$\mathcal{L}_t^{\text{cross}} = \sum_{(J^l, J^r) \in \mathcal{J}_t^{\text{foot}}} \mathbb{1}_{\geq \delta} \cdot \exp(-\|(J^l - J^r)\|, \tag{7}$$

which penalizes overly close joint pairs from opposite legs to ensure physically plausible and natural leg motion. Here,  $\mathcal{J}_t^{foot}$  denotes a predefined set of joint pairs corresponding to the left and right legs, and  $\mathbb{1}_{\geq \delta}$  is an indicator function that outputs 1 when  $\exp(-\|(J^l-J^r)\|)$  exceeds threshold  $\delta$ , and 0 otherwise.

**Shape & Pose Prior Loss** To impose structural and kinematic constraints on the deformed mesh, we follow Rüegg et al. [2022]; Zuffi et al. [2017] and apply a prior loss defined as:

$$\mathcal{L}^{\text{prior}} = \mathcal{L}^{\text{shape}} + \sum_{t=1}^{T} \mathcal{L}_{t}^{\text{pose}}.$$
 (8)

The shape prior term  $\mathcal{L}_t^{\text{shape}}$  encourages the D-SMAL shape coefficients  $\beta$  to match a prior distribution. The pose prior term  $\mathcal{L}_t^{\text{pose}}$  constrains the estimated D-SMAL pose parameters  $\theta_t$  to remain within plausible limits by applying a Gaussian prior penalty. Details are presented in *Appendix*.

#### 4.2.3 Stage 3: Temporal Refinement.

While the previous loss terms are computed independently for each frame, they do not enforce temporal consistency across the sequence. The third stage incorporates a Temporal Smoothness Loss, in addition to the above comprehensive frame-wise losses, to further refine the motion sequence:

$$\mathcal{L}^{\text{temp}} = \sum_{t=1}^{T-1} \sum_{k=1}^{|\mathcal{J}|} (\|\mathcal{J}_{t+1}^k - \mathcal{J}_t^k\| + \|\mathcal{R}(\mathcal{J}_{t+1}^k) - \mathcal{R}(\mathcal{J}_t^k)\|),$$
(9)

which penalizes abrupt changes in both 3D joint positions and their 2D projections.

# 4.3 Implementation Details

**Method Usage Across Different Settings** In the first and second stages, the loss is computed by averaging over mini-batches of frames sampled from video sequences. In the third stage, motion is further refined by optimizing over a sampled continuous sequence segment. Based on **DogMo**, we establish four evaluation setups for motion recovery. For setups involving multi-view inputs, we average the loss across all views. The key difference between setups with and without depth input lies in using Chamfer Depth Loss, which is applied only when depth data is available.

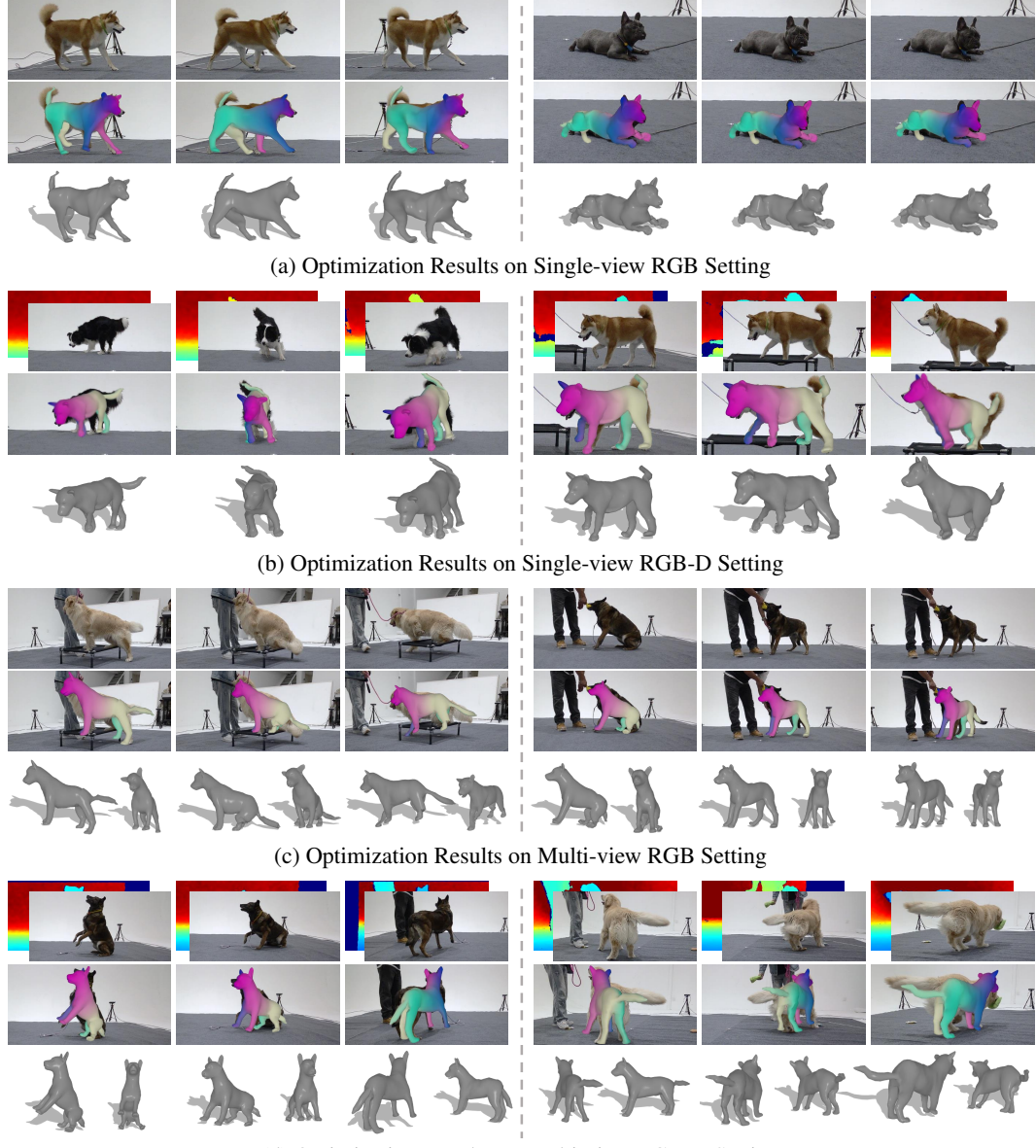
**Hyperparameter Configurations** In our implementation, we employ two separate MLPs to map the time-varying global translation and orientation, as well as body pose, *i.e.*, MLP<sub>TR</sub> and MLP<sub> $\theta$ </sub>. MLP<sub>TR</sub> consists of 3 layers with 16 hidden units per layer, while MLP<sub> $\theta$ </sub> has 3 layers with 64 hidden units per layer. The number of optimization steps is the product of a specified multiplier and the frame number. For single-view sequences, we set the multipliers as 5, 20, and 5 for the first, second, and third stages, respectively; for multi-view sequences, the corresponding multipliers are 10, 25, and 5. We perform optimization using the Adam optimizer. All experiments are implemented in PyTorch and run on a single NVIDIA GeForce RTX 4090 GPU. Refer to *Appendix* for more details.

#### 5 Experiments

# 5.1 Evaluation Setup

**Metrics** We evaluate the methods using six metrics: (1) IoU, the Intersection-over-Union between the rendered silhouette of the estimated SMAL model and the ground-truth dog segmentation; (2)  $IoU_{w5}$ , the average IoU over the worst 5% of frames in each sequence, reflecting the method's robustness; (3) F-score [Wang et al., 2018], which quantifies the distance between the estimated dog mesh and the inverse-projected dog point cloud from RGB-D images; (4)  $Pene_{\%}$ , the proportion of mesh vertices that penetrate the floor over a sequence; (5) Jitter (m), measuring temporal smoothness; and (6) Foot Skating (FS) (m), which evaluates the naturalness of foot contact by capturing sliding artifacts. Given that the F-score measures 3D reconstruction accuracy, we adopt it as the primary evaluation metric. The computation details of these metrics are presented in Appendix.

**Baselines** To the best of our knowledge, there are no open-source baselines available for dog motion recovery from multi-view or RGB-D videos. We adopt SMALify [Biggs et al., 2020], a learning-based method that estimates dog pose from monocular RGB images, as the baseline for comparison on the single-view RGB setting. We use the officially released model and checkpoint to evaluate on our dataset. We also compare against AnimalAvatar [Sabathier et al., 2024], an optimization-based method originally designed for recovering a dog model from single-view RGB video sequences, which we further adapt to handle RGB-D input. We use the default model configuration and hyperparameters.



(d) Optimization Results on Multi-view RGB-D Setting

Figure 5: **Qualitative results.** Each benchmark setting shows two results, with three sampled frames per result from left to right. Three rows show the input image, CSE model projection, and recovered mesh, respectively. In multi-view settings, we show only one input view for clarity and visualize the mesh from two angles.

In addition, we include two ablated variants of our pipeline, *w/o stage 1* and *w/o stage 3*, to assess the contribution of coarse alignment initialization and temporal refinement, respectively.

## 5.2 Results

**Qualitative Results** Fig. 5 shows the qualitative results of our method across the four setups. Our method effectively recovers dog motion from various input types, ranging from single-view to multi-view and from RGB to RGB-D inputs.

**Quantitative Results** We present the quantitative results in Tab. 2, from which we draw the following several key observations.

Although the models under the single-view RGB setting achieve higher IoU scores, they consistently
perform significantly worse in terms of F-score, Pene<sub>%</sub>, Jitter, and Foot Skating. This discrepancy
suggests that single-view RGB lacks sufficient 3D cues to recover absolute body shape and position

Table 2.	Quantitative	reculte Ro	Id indicates	the best result.
Table 2.	Quantitative	i counts, Du	na maicates	THE DEST LESUIT.

Method		Single-view RGB						Single-view RGB-D				
Method	IoU↑	IoU <sub>w5</sub> ↑	F-score ↑	Pene <sub>%</sub> ↓	Jitter ↓	FS ↓	IoU↑	IoU <sub>w5</sub> ↑	F-score ↑	Pene <sub>%</sub> ↓	Jitter ↓	FS ↓
SMALify	0.6133	0.4058	0.2324	0.4363	0.0895	0.0435	-	-	-	-	-	-
AnimalAvatar	0.6116	0.5197	0.0283	0.2702	0.0298	0.0144	0.6036	0.4905	0.4748	0.2039	0.0260	0.0184
w/o stage 1 (Ours)	0.6024	0.4842	0.3360	-	-	-	0.6074	0.4901	0.6619	-	-	-
w/o stage 3 (Ours)	0.6491	0.5235	0.3576	0.3698	0.0211	0.0366	0.6424	0.5235	0.7666	0.1261	0.0140	0.0167
Full (Ours)	0.6505	0.5247	0.3593	0.3653	0.0206	0.0361	0.6414	0.5228	0.7673	0.1278	0.0137	0.0166
Method	Multi-view RGB					Multi-view RGB-D						
Method	IoU↑	IoU <sub>w5</sub> ↑	F-score ↑	Pene <sub>%</sub> ↓	Jitter ↓	FS ↓	IoU↑	IoU <sub>w5</sub> ↑	F-score ↑	Pene <sub>%</sub> ↓	Jitter ↓	FS ↓
w/o stage 1 (Ours)	0.6084	0.4358	0.9096	-	-	-	0.6122	0.4403	0.9134	-	-	-
w/o stage 3 (Ours)	0.6271	0.4496	0.9107	0.0700	0.0124	0.0188	0.6300	0.4557	0.9137	0.0699	0.0123	0.0188
Full (Ours)	0.6258	0.4490	0.9107	0.0688	0.0120	0.0188	0.6286	0.4549	0.9137	0.0687	0.0119	0.0187

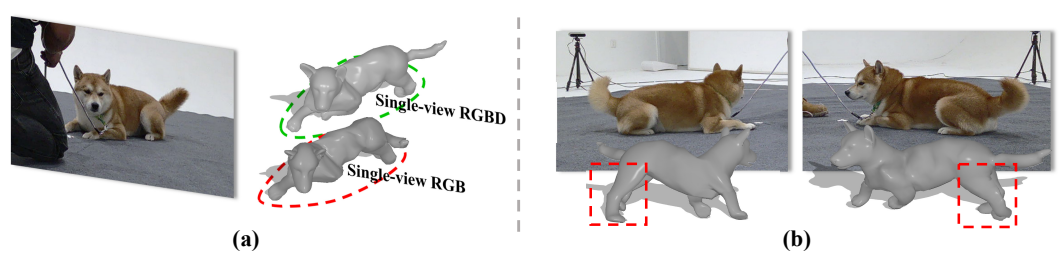


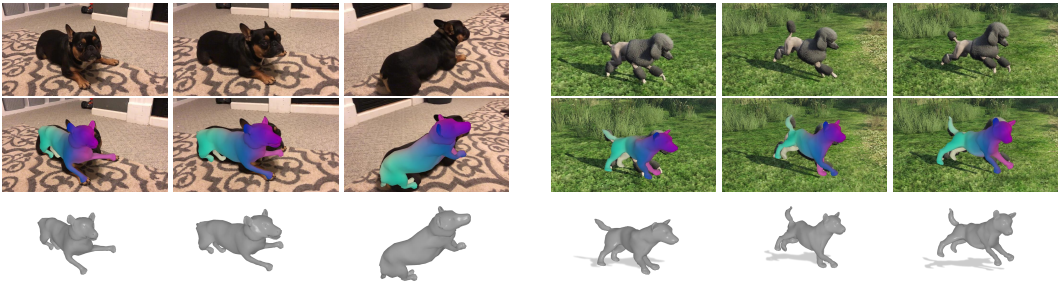
Figure 6: **Ambiguity in dog mesh recovery.** (a) Without real 3D information, the optimization method using only single-view RGB input fails to recover the dog's absolute position and size accurately. (b) The resulting mesh also exhibits noticeable artifacts when viewed from other perspectives.

accurately in 3D space. In contrast, multi-view and depth inputs provide richer spatial information, enabling more precise reconstruction of 3D shape and position. These results are consistent with the qualitative visualizations in Fig. 6.

- Our method significantly outperforms SMALify [Biggs et al., 2020] and AnimalAvatar [Sabathier et al., 2024] across IoU and F-score, demonstrating that these baselines struggle to accurately fit dog silhouettes and recover global 3D positions and body sizes. Although AnimalAvatar uses a similar optimization strategy, its reliance on the original D-SMAL model limits its ability to handle large variations in dog body sizes. Its one-stage, frame-independent optimization also lacks proper initialization and temporal constraints, often yielding suboptimal results. While AnimalAvatar yields better Pene<sub>%</sub> and Foot Skating, this is primarily because it produces meshes that float above the floor. Such non-contact meshes naturally result in zero penetration and foot skating, which spuriously improve these metrics.
- The first-stage coarse alignment is crucial for motion recovery, particularly in the single-view RGB-D setting, as it provides favorable initialization and prevents suboptimal in the subsequent dense optimization. We also observe that varying the initial value of s greatly affects the results of the model w/o stage 1, especially for Pene<sub>%</sub>, Jitter, and FS; therefore, we omit these results in Tab. 2. Additional analysis is provided in Appendix. The third-stage temporal refinement further improves the final results in the single-view RGB setting, and its impact diminishes in multi-view or depth-rich scenarios, where the input provides sufficient information for accurate recovery.

In the setting of motion recovery from single-view RGB video, the absence of real 3D information introduces ambiguity in the reconstructed dog mesh, *i.e.*, the estimated results cannot reliably determine the true position and size of the dog. As shown in Fig. 6, we compare results from the same recording using single-view RGB and single-view RGB-D inputs. The reconstruction from single-view RGB shows clear deviations in body position and size compared to that using inputs with 3D cues, which aligns with the F-score results reported in Tab. 2. Besides, the resulting mesh from single-view RGB input also exhibits noticeable artifacts when viewed from other perspectives.

**Generalization** We emphasize that although our method adopts an instance-specific optimization pipeline, it generalizes well across diverse cases. This generalization stems from its reliance on dog masks and keypoints predicted by pretrained models, *i.e.*, Grounded SAM 2 [Ren et al., 2024], which are known for strong robustness across varied scenarios. In addition, the carefully designed cost functions are broadly applicable, as they are independent of specific pixel values and remain effective across different instances. To further demonstrate this, we evaluate our method on the CoP3D [Sinha et al., 2023] and DigiDogs [Shooter et al., 2024a] datasets, which feature in-the-wild scenes. Since



(a) Results on COP3D

(b) Results on DigiDogs

Figure 7: **Generalization results.** We further evaluate our method on (a) COP3D [Sinha et al., 2023] and (b) DigiDogs [Shooter et al., 2024a] datasets, which feature in-the-wild scenes.

Table 3: **Optimization efficiency.** Optimization time (in minutes) required by each model. Lower is better.

Method	Setting	Stage 1	Stage 2	Stage 3	Total	Setting	Stage 1	Stage 2	Stage 3	Total
	Single-view RGB Single-view RGB		12.70			Single-view RGB-D Single-view RGB-D				117.47 $19.25$
Ours	Multi-view RGB	19.82	53.12	11.22	84.16	Multi-view RGB-D	20.38	54.52	11.45	86.35

neither dataset provides multi-view imaging, we conduct only single-view evaluations: RGB setting on CoP3D and RGB-D setting on DigiDogs, respectively. Qualitative results are shown in Fig. 7. For quantitative results, our method achieves IoU 0.7190 and IoU $_{w5}$  0.5912 on CoP3D, and IoU 0.6644, IoU $_{w5}$  0.5832, and F-score 0.7946 on DigiDogs, which are slightly higher than those on **DogMo**. We attribute this improvement to two factors: (1) the dog motions in CoP3D are predominantly sprawling with limited variation, making them easier to optimize; and (2) DigiDogs is a synthetic dataset with minimal observation noise, enabling more accurate reconstruction.

**Optimization Efficiency** To evaluate optimization efficiency, we report the runtime of our model for each stage and the entire pipeline, as shown in Tab. 3. Most computation is spent in the second stage, which involves all optimization terms and requires more iterations. The cost further increases with multi-view observations. Notably, our method converges in fewer iterations than AnimalAvatar [Sabathier et al., 2024], resulting in shorter overall runtime. This improvement stems from the strong initialization in the first stage and the use of a scaling parameter that resizes the body mesh, effectively reducing the optimization space in the second stage.

#### 5.3 Discussion

**Limitations** While *DogMo* makes significant contributions, it is collected in a controlled indoor lab scenario, lacking the diversity and complexity of in-the-wild scenes. This limits the generalization of learning-based models trained solely on *DogMo*, particularly in scenarios with complex backgrounds, varying lighting, or occlusions. On the algorithmic side, although our optimization pipeline is effective, it remains computationally intensive, posing challenges for real-time or large-scale deployment.

**Future Works** In future work, we aim to scale up *DogMo* to support more robust and generalizable modeling of dog motion. This expansion includes augmenting the dataset with photorealistic, in-the-wild backgrounds using advanced rendering and simulation tools. Beyond data augmentation, the expanded dataset will enable two research directions: (1) incorporating physics-based constraints to enable physically plausible motion recovery, and (2) leveraging generative models to learn data-driven motion priors for diverse motion synthesis [Yang et al., 2024; Wang et al., 2025] and prediction tasks.

#### 6 Conclusion

This work introduces DogMo, a large-scale multi-view RGB-D dataset for 4D canine motion recovery. DogMo features 5 cameras capturing the movements of 10 dogs across 11 action types, resulting in 1.2k motion clips spanning over 220 minutes. Built upon this dataset, we establish four motion recovery benchmark settings to encourage future research. We also propose a unified three-stage optimization pipeline that recovers the dog's body parameters in a coarse-to-fine manner, from single-view to multi-view and from RGB to RGB-D inputs. We believe our work lays a strong foundation for advancing understanding of animal motion, with promising applications in animation and VR/AR.

**Acknowlwdgement** This work is supported in part by the National Natural Science Foundation of China (NSFC) (62172043).

#### References

- Aygun, M. and Mac Aodha, O. (2024). Saor: Single-view articulated object reconstruction. In *Conference on Computer Vision and Pattern Recognition (CVPR)*. 3
- Badger, M., Wang, Y., Modh, A., Perkes, A., Kolotouros, N., Pfrommer, B. G., Schmidt, M. F., and Daniilidis, K. (2020). 3d bird reconstruction: a dataset, model, and shape recovery from a single view. In *European Conference on Computer Vision (ECCV)*. 3
- Bala, P. C., Eisenreich, B. R., Yoo, S. B. M., Hayden, B. Y., Park, H. S., and Zimmermann, J. (2020). Automated markerless pose estimation in freely moving macaques with openmonkeystudio. *Nature Communications*, 11(1):4560.
- Biggs, B., Boyne, O., Charles, J., Fitzgibbon, A., and Cipolla, R. (2020). Who left the dogs out? 3d animal reconstruction with expectation maximization in the loop. In *European Conference on Computer Vision* (ECCV). 2, 3, 7, 9, 17
- Biggs, B., Roddick, T., Fitzgibbon, A., and Cipolla, R. (2019). Creatures great and smal: Recovering the shape and motion of animals from video. In *Asian Conference on Computer Vision (ACCV)*. 2, 3
- Black, M. J., Patel, P., Tesch, J., and Yang, J. (2023). Bedlam: A synthetic dataset of bodies exhibiting detailed lifelike animated motion. In *Conference on Computer Vision and Pattern Recognition (CVPR)*. 2
- Bogo, F., Kanazawa, A., Lassner, C., Gehler, P., Romero, J., and Black, M. J. (2016). Keep it smpl: Automatic estimation of 3d human pose and shape from a single image. In *European Conference on Computer Vision (ECCV)*. 2
- Bradski, G. (2000). The opency library. *Dr. Dobb's Journal: Software Tools for the Professional Programmer*, 25(11):120–123. 4
- Cao, J., Tang, H., Fang, H.-S., Shen, X., Lu, C., and Tai, Y.-W. (2019). Cross-domain adaptation for animal pose estimation. In *International Conference on Computer Vision (ICCV)*. 3
- Cashman, T. J. and Fitzgibbon, A. W. (2012). What shape are dolphins? building 3d morphable models from 2d images. *Transactions on Pattern Analysis and Machine Intelligence (TPAMI)*, 35(1):232–244. 3
- Deane, J., Kearney, S., Kim, K. I., and Cosker, D. (2024). Rgbt-dog: A parametric model and pose prior for canine body analysis data creation. In *Proceedings of Winter Conference on Applications of Computer Vision (WACV)*. 3
- Ho, J., Jain, A., and Abbeel, P. (2020). Denoising diffusion probabilistic models. In *Advances in Neural Information Processing Systems (NeurIPS)*. 3
- Ionescu, C., Papava, D., Olaru, V., and Sminchisescu, C. (2013). Human3. 6m: Large scale datasets and predictive methods for 3d human sensing in natural environments. *Transactions on Pattern Analysis and Machine Intelligence (TPAMI)*, 36(7):1325–1339.
- Joska, D., Clark, L., Muramatsu, N., Jericevich, R., Nicolls, F., Mathis, A., Mathis, M. W., and Patel, A. (2021). Acinoset: a 3d pose estimation dataset and baseline models for cheetahs in the wild. In *International Conference on Robotics and Automation (ICRA)*. 3
- Kanazawa, A., Black, M. J., Jacobs, D. W., and Malik, J. (2018). End-to-end recovery of human shape and pose. In Conference on Computer Vision and Pattern Recognition (CVPR). 2
- Kearney, S., Li, W., Parsons, M., Kim, K. I., and Cosker, D. (2020). Rgbd-dog: Predicting canine pose from rgbd sensors. In *Conference on Computer Vision and Pattern Recognition (CVPR)*. 2, 3, 4
- Khosla, A., Jayadevaprakash, N., Yao, B., and Li, F.-F. (2011). Novel dataset for fine-grained image categorization: Stanford dogs. In Conference on Computer Vision and Pattern Recognition Workshop (CVPRW).
  3
- Li, C., Ghorbani, N., Broomé, S., Rashid, M., Black, M. J., Hernlund, E., Kjellström, H., and Zuffi, S. (2021). hsmal: Detailed horse shape and pose reconstruction for motion pattern recognition. *arXiv* preprint *arXiv*:2106.10102. 3

- Li, C. and Lee, G. H. (2021). Coarse-to-fine animal pose and shape estimation. In *Advances in Neural Information Processing Systems (NeurIPS)*. 3
- Li, C., Mellbin, Y., Krogager, J., Polikovsky, S., Holmberg, M., Ghorbani, N., Black, M. J., Kjellström, H., Zuffi, S., and Hernlund, E. (2024a). The poses for equine research dataset (pferd). *Scientific Data*, 11(1):497. 3
- Li, C., Yang, Y., Weng, Z., Hernlund, E., Zuffi, S., and Kjellström, H. (2024b). Dessie: Disentanglement for articulated 3d horse shape and pose estimation from images. In *Asian Conference on Computer Vision (ACCV)*.
- Li, S., Li, J., Tang, H., Qian, R., and Lin, W. (2020). Atrw: A benchmark for amur tiger re-identification in the wild. In *ACM International Conference on Multimedia (MM)*. 3
- Li, Z., Litvak, D., Li, R., Zhang, Y., Jakab, T., Rupprecht, C., Wu, S., Vedaldi, A., and Wu, J. (2024c). Learning the 3d fauna of the web. In *Conference on Computer Vision and Pattern Recognition (CVPR)*. 3
- Li, Z., Liu, J., Zhang, Z., Xu, S., and Yan, Y. (2022). Cliff: Carrying location information in full frames into human pose and shape estimation. In *European Conference on Computer Vision (ECCV)*. 2
- Liu, D., Hou, J., Huang, S., Liu, J., He, Y., Zheng, B., Ning, J., and Zhang, J. (2023a). Lote-animal: A long time-span dataset for endangered animal behavior understanding. In *International Conference on Computer Vision (ICCV)*. 3
- Liu, D., Stathopoulos, A., Zhangli, Q., Gao, Y., and Metaxas, D. (2023b). Lepard: Learning explicit part discovery for 3d articulated shape reconstruction. In *Advances in Neural Information Processing Systems* (NeurIPS). 3
- Liu, R., Wu, R., Van Hoorick, B., Tokmakov, P., Zakharov, S., and Vondrick, C. (2023c). Zero-1-to-3: Zero-shot one image to 3d object. In *International Conference on Computer Vision (ICCV)*. 3
- Luo, H., Xu, T., Jiang, Y., Zhou, C., Qiu, Q., Zhang, Y., Yang, W., Xu, L., and Yu, J. (2022). Artemis: articulated neural pets with appearance and motion synthesis. *ACM Transactions on Graphics (TOG)*, 41(4):1–19. 2, 3
- Lyu, J., Zhu, T., Gu, Y., Lin, L., Cheng, P., Liu, Y., Tang, X., and An, L. (2024). Animer: Animal pose and shape estimation using family aware transformer. *arXiv preprint arXiv:2412.00837*. 3
- Ma, X., Kaufhold, S., Su, J., Zhu, W., Terwilliger, J., Meza, A., Zhu, Y., Rossano, F., and Wang, Y. (2023). Chimpact: A longitudinal dataset for understanding chimpanzee behaviors. In *Advances in Neural Information Processing Systems (NeurIPS)*. 3
- Mahmood, N., Ghorbani, N., Troje, N. F., Pons-Moll, G., and Black, M. J. (2019). Amass: Archive of motion capture as surface shapes. In *International Conference on Computer Vision (ICCV)*.
- Marshall, J., Klibaite, U., gellis, a., Aldarondo, D., Olveczky, B., and Dunn, T. W. (2021). The pair-r24m dataset for multi-animal 3d pose estimation. In *Proceedings of the Neural Information Processing Systems (NeurIPS) Track on Datasets and Benchmarks*. 3
- Mu, J., Qiu, W., Hager, G. D., and Yuille, A. L. (2020). Learning from synthetic animals. In Conference on Computer Vision and Pattern Recognition (CVPR). 3
- Muramatsu, N., da Silva, Z., Joska, D., Nicolls, F., and Patel, A. (2022). Improving 3d markerless pose estimation of animals in the wild using low-cost cameras. In *International Conference on Intelligent Robots and Systems (IROS)*. 3
- Naik, H., Chan, A. H. H., Yang, J., Delacoux, M., Couzin, I. D., Kano, F., and Nagy, M. (2023). 3d-pop-an automated annotation approach to facilitate markerless 2d-3d tracking of freely moving birds with marker-based motion capture. In *Conference on Computer Vision and Pattern Recognition (CVPR)*. 3
- Neverova, N., Novotny, D., Szafraniec, M., Khalidov, V., Labatut, P., and Vedaldi, A. (2020). Continuous surface embeddings. In *Advances in Neural Information Processing Systems (NeurIPS)*. 2, 6
- Ng, X. L., Ong, K. E., Zheng, Q., Ni, Y., Yeo, S. Y., and Liu, J. (2022). Animal kingdom: A large and diverse dataset for animal behavior understanding. In *Conference on Computer Vision and Pattern Recognition (CVPR)*. 3
- Patel, M., Gu, Y., Carstensen, L. C., Hasselmo, M. E., and Betke, M. (2023). Animal pose tracking: 3d multimodal dataset and token-based pose optimization. *International Journal of Computer Vision (IJCV)*, 131(2):514–530. 3

- Poole, B., Jain, A., Barron, J. T., and Mildenhall, B. (2023). Dreamfusion: Text-to-3d using 2d diffusion. In *International Conference on Learning Representations (ICLR)*. 3
- Qian, G., Mai, J., Hamdi, A., Ren, J., Siarohin, A., Li, B., Lee, H.-Y., Skorokhodov, I., Wonka, P., Tulyakov, S., et al. (2024). Magic123: One image to high-quality 3d object generation using both 2d and 3d diffusion priors. In *International Conference on Learning Representations (ICLR)*. 3
- Ren, T., Liu, S., Zeng, A., Lin, J., Li, K., Cao, H., Chen, J., Huang, X., Chen, Y., Yan, F., et al. (2024). Grounded sam: Assembling open-world models for diverse visual tasks. *arXiv* preprint arXiv:2401.14159. 5, 9
- Rombach, R., Blattmann, A., Lorenz, D., Esser, P., and Ommer, B. (2022). High-resolution image synthesis with latent diffusion models. In *Conference on Computer Vision and Pattern Recognition (CVPR)*. 3
- Rüegg, N., Tripathi, S., Schindler, K., Black, M. J., and Zuffi, S. (2023). Bite: Beyond priors for improved three-d dog pose estimation. In *Conference on Computer Vision and Pattern Recognition (CVPR)*. 3, 4
- Rüegg, N., Zuffi, S., Schindler, K., and Black, M. J. (2022). Barc: Learning to regress 3d dog shape from images by exploiting breed information. In *Conference on Computer Vision and Pattern Recognition (CVPR)*. 2, 3, 6, 7, 15
- Sabathier, R., Mitra, N. J., and Novotny, D. (2024). Animal avatars: Reconstructing animatable 3d animals from casual videos. In *European Conference on Computer Vision (ECCV)*. 2, 3, 5, 6, 7, 9, 10, 17
- Shi, Y., Wang, P., Ye, J., Long, M., Li, K., and Yang, X. (2024). Mvdream: Multi-view diffusion for 3d generation. In *International Conference on Learning Representations (ICLR)*. 3
- Shin, S., Kim, J., Halilaj, E., and Black, M. J. (2024). Wham: Reconstructing world-grounded humans with accurate 3d motion. In *Conference on Computer Vision and Pattern Recognition (CVPR)*. 2
- Shooter, M., Malleson, C., and Hilton, A. (2024a). Digidogs: Single-view 3d pose estimation of dogs using synthetic training data. In *Proceedings of Winter Conference on Applications of Computer Vision (WACV)*. 2, 3, 4, 9, 10
- Shooter, M., Malleson, C., and Hilton, A. (2024b). Sydog-video: A synthetic dog video dataset for temporal pose estimation. *International Journal of Computer Vision (IJCV)*, 132(6):1986–2002. 2, 3, 4
- Sinha, S., Shapovalov, R., Reizenstein, J., Rocco, I., Neverova, N., Vedaldi, A., and Novotny, D. (2023). Common pets in 3d: Dynamic new-view synthesis of real-life deformable categories. In *Conference on Computer Vision and Pattern Recognition (CVPR)*. 3, 4, 9, 10
- Sosa, J. and Hogg, D. (2023). A horse with no labels: Self-supervised horse pose estimation from unlabelled images and synthetic prior. In *Conference on Computer Vision and Pattern Recognition (CVPR)*. 3
- Tan, J., Yang, G., and Ramanan, D. (2023). Distilling neural fields for real-time articulated shape reconstruction. In Conference on Computer Vision and Pattern Recognition (CVPR). 3
- Tu, T., Li, M.-F., Lin, C. H., Cheng, Y.-C., Sun, M., and Yang, M.-H. (2025). Dreamo: articulated 3d reconstruction from a single casual video. In *Proceedings of Winter Conference on Applications of Computer Vision (WACV)*. 3
- Von Marcard, T., Henschel, R., Black, M. J., Rosenhahn, B., and Pons-Moll, G. (2018). Recovering accurate 3d human pose in the wild using imus and a moving camera. In *European Conference on Computer Vision (ECCV)*. 2
- Wang, N., Zhang, Y., Li, Z., Fu, Y., Liu, W., and Jiang, Y.-G. (2018). Pixel2mesh: Generating 3d mesh models from single rgb images. In European Conference on Computer Vision (ECCV). 7, 15
- Wang, X., Ruan, K., Zhang, X., and Wang, G. (2025). Animo: Species-aware model for text-driven animal motion generation. In *CVPR*. 10
- Wang, Y., Kolotouros, N., Daniilidis, K., and Badger, M. (2021). Birds of a feather: Capturing avian shape models from images. In *Conference on Computer Vision and Pattern Recognition (CVPR)*. 3
- Wu, S., Jakab, T., Rupprecht, C., and Vedaldi, A. (2023a). Dove: Learning deformable 3d objects by watching videos. *International Journal of Computer Vision*, 131(10):2623–2634. 3
- Wu, S., Li, R., Jakab, T., Rupprecht, C., and Vedaldi, A. (2023b). Magicpony: Learning articulated 3d animals in the wild. In *Conference on Computer Vision and Pattern Recognition (CVPR)*. 3

- Wu, Y., Chen, Z., Liu, S., Ren, Z., and Wang, S. (2022). Casa: Category-agnostic skeletal animal reconstruction. In Advances in Neural Information Processing Systems (NeurIPS). 3
- Xu, J., Zhang, Y., Peng, J., Ma, W., Jesslen, A., Ji, P., Hu, Q., Zhang, J., Liu, Q., Wang, J., et al. (2023). Animal3d: A comprehensive dataset of 3d animal pose and shape. In *International Conference on Computer Vision (ICCV)*. 3
- Yang, G., Bajcsy, A., Saito, S., and Kanazawa, A. (2025). Agent-to-sim: Learning interactive behavior models from casual longitudinal videos. In *International Conference on Learning Representations (ICLR)*. 3
- Yang, G., Sun, D., Jampani, V., Vlasic, D., Cole, F., Chang, H., Ramanan, D., Freeman, W. T., and Liu, C. (2021).
  Lasr: Learning articulated shape reconstruction from a monocular video. In *Conference on Computer Vision and Pattern Recognition (CVPR)*. 3
- Yang, G., Vo, M., Neverova, N., Ramanan, D., Vedaldi, A., and Joo, H. (2022a). Banmo: Building animatable 3d neural models from many casual videos. In Conference on Computer Vision and Pattern Recognition (CVPR).
- Yang, G., Yang, S., Zhang, J. Z., Manchester, Z., and Ramanan, D. (2023). Ppr: Physically plausible reconstruction from monocular videos. In *International Conference on Computer Vision (ICCV)*. 2, 3
- Yang, Y., Yang, J., Xu, Y., Zhang, J., Lan, L., and Tao, D. (2022b). Apt-36k: A large-scale benchmark for animal pose estimation and tracking. In *Advances in Neural Information Processing Systems (NeurIPS)*. 2, 3
- Yang, Z., Zhou, M., Shan, M., Wen, B., Xuan, Z., Hill, M., Bai, J., Qi, G.-J., and Wang, Y. (2024). Omnimotiongpt: Animal motion generation with limited data. In *Conference on Computer Vision and Pattern Recognition* (CVPR). 10
- Yao, C.-H., Raj, A., Hung, W.-C., Rubinstein, M., Li, Y., Yang, M.-H., and Jampani, V. (2023a). Artic3d: Learning robust articulated 3d shapes from noisy web image collections. In *Advances in Neural Information Processing Systems (NeurIPS)*. 3
- Yao, Y., Bala, P., Mohan, A., Bliss-Moreau, E., Coleman, K., Freeman, S. M., Machado, C. J., Raper, J., Zimmermann, J., Hayden, B. Y., et al. (2023b). Openmonkeychallenge: dataset and benchmark challenges for pose estimation of non-human primates. *International Journal of Computer Vision (IJCV)*, 131(1):243–258.
- Ye, S., Filippova, A., Lauer, J., Schneider, S., Vidal, M., Qiu, T., Mathis, A., and Mathis, M. W. (2024). Superanimal pretrained pose estimation models for behavioral analysis. *Nature Communications*, 15(1):5165.
- Yu, H., Xu, Y., Zhang, J., Zhao, W., Guan, Z., and Tao, D. (2021). Ap-10k: A benchmark for animal pose estimation in the wild. In Proceedings of the Neural Information Processing Systems (NeurIPS) Track on Datasets and Benchmarks. 2, 3
- Zeng, D., Zhu, Y., Li, S., Zhao, Q., Shen, Q., and Tang, B. (2024). Towards labeling-free fine-grained animal pose estimation. In *ACM International Conference on Multimedia (MM)*. 3
- Zuffi, S., Kanazawa, A., Berger-Wolf, T., and Black, M. J. (2019). Three-d safari: Learning to estimate zebra pose, shape, and texture from images" in the wild". In *International Conference on Computer Vision (ICCV)*.
- Zuffi, S., Kanazawa, A., Jacobs, D. W., and Black, M. J. (2017). 3d menagerie: Modeling the 3d shape and pose of animals. In *Conference on Computer Vision and Pattern Recognition (CVPR)*. 2, 3, 4, 7, 15
- Zuffi, S., Mellbin, Y., Li, C., Hoeschle, M., Kjellström, H., Polikovsky, S., Hernlund, E., and Black, M. J. (2024).
  Varen: Very accurate and realistic equine network. In *Conference on Computer Vision and Pattern Recognition (CVPR)*.

# **Appendix**

# A Additional Details

## A.1 Optimization

**Optimization Rate** We set different optimization rates (*i.e.*, learning rates) for different parameters during the optimization. In the first stage, we initialize the optimization rates as follows:  $5e^{-3}$  for the scale parameter and  $5e^{-2}$  for the parameters of  $\mathrm{MLP}_{TR}$ . In the second stage, we set the optimization rates to  $5e^{-5}$  for the scale parameter,  $5e^{-2}$  for the shape parameter, and  $5e^{-4}$  for both  $\mathrm{MLP}_{TR}$  and  $\mathrm{MLP}_{\theta}$ . In the third stage, we set the optimization rates to  $1e^{-5}$  for both  $\mathrm{MLP}_{TR}$  and  $\mathrm{MLP}_{\theta}$ . All optimization rates follow a step-wise decay schedule: at 75% and 93.75% of the total optimization steps, the rate is multiplied by a factor of 0.3.

**Loss Weight** For each optimization loss term, we set the loss weight as follows: 400.0 for  $\mathcal{L}_t^{\mathrm{mask}}$ , 60.0 for  $\mathcal{L}_t^{\mathrm{kp}}$ , 1.0 for  $\mathcal{L}_t^{\mathrm{depth}}$ , 20.0 for  $\mathcal{L}_t^{\mathrm{cross}}$ , 2.5 for  $\mathcal{L}_t^{\mathrm{cross}}$ , 0.005 for  $\mathcal{L}_t^{\mathrm{prior}}$ , and 0.1 for  $\mathcal{L}_t^{\mathrm{temp}}$ .

#### A.2 Shape & Pose Prior Loss

To enhance the plausibility of the estimated results and mitigate implausible joint poses or abnormal body proportions, we incorporate two prior constraint losses following existing studies [Rüegg et al., 2022; Zuffi et al., 2017]: a pose prior loss and a shape prior loss. These priors are modeled as Gaussian distributions derived from the statistical properties of animal datasets. The Mahalanobis distance is employed during optimization to regularize the parameters, guiding the SMAL predictions toward anatomically consistent pose and body shape distributions.

**Shape Prior Loss** The shape prior loss  $\mathcal{L}^{shape}$  consists of two components: a body shape prior loss  $\mathcal{L}^{body}$  and a limb proportion prior loss  $\mathcal{L}^{limb}$ . The body shape prior loss  $\mathcal{L}^{body}$  is derived from a Gaussian prior fitted to the body shape parameters in the BARC [Rüegg et al., 2022] dataset. Here,  $\mu_{body}$  and  $\Sigma_{body}$  represent the mean vector and the positive semi-definite covariance matrix computed from the data. The Mahalanobis distance between the optimized shape vector  $\boldsymbol{\beta}$  and the prior distribution is then given by

$$\mathcal{L}^{\text{body}} = (\boldsymbol{\beta} - \boldsymbol{\mu}_{\text{body}})^{\top} \boldsymbol{\Sigma}_{\text{body}}^{-1} (\boldsymbol{\beta} - \boldsymbol{\mu}_{\text{body}}). \tag{A1}$$

To further ensure reasonable limb proportions, we introduce a limb proportion prior loss  $\mathcal{L}^{\text{limb}}$ , which applies a weighted quadratic penalty to limb-related shape coefficients, *i.e.*,

$$\mathcal{L}^{\text{limb}} = \left\| \mathbf{w} \odot \boldsymbol{\beta}^{\text{limb}} \right\|_{2}^{2},\tag{A2}$$

where  $\mathbf{w}$  is a manually defined weight vector. The final shape prior loss combines the body and limb prior terms through a weighted sum, i.e.,  $\mathcal{L}^{\text{shape}} = w_{\text{body}} \cdot \mathcal{L}^{\text{body}} + w_{\text{limb}} \cdot \mathcal{L}^{\text{limb}}$ .

**Pose Prior Loss** Similarly, we model the joint rotation prior as a Gaussian distribution characterized by the mean vector  $\mu_{pose}$  and a positive semi-definite covariance matrix  $\Sigma_{pose}$ . The Mahalanobis distance between the optimized pose vector and this prior distribution is then computed as

$$\mathcal{L}_t^{\text{pose}} = (\theta_t - \boldsymbol{\mu}_{\text{pose}})^{\top} \boldsymbol{\Sigma}_{\text{pose}}^{-1} (\theta_t - \boldsymbol{\mu}_{\text{pose}}). \tag{A3}$$

## A.3 Metric Computation

**F-score** Following Wang et al. [2018], we first uniformly sample points from our optimization result and lift the masked depth image pixels into 3D space. We calculate precision and recall by measuring the percentage of points from the optimization or the depth image reprojection that have a nearest neighbor in the other set within a specified threshold. We set the threshold as 0.05. The F-score is then computed as the harmonic mean of precision and recall.

 $Pene_{\%}$  We compute the penetration ratio as the proportion of SMAL mesh vertices that penetrate the ground plane in each frame.

**Jitter** The jitter metric quantifies the temporal smoothness of predicted SMAL joint trajectories, indicating the stability of the motion. It is calculated as the mean second-order difference of all joint positions across the sequence.

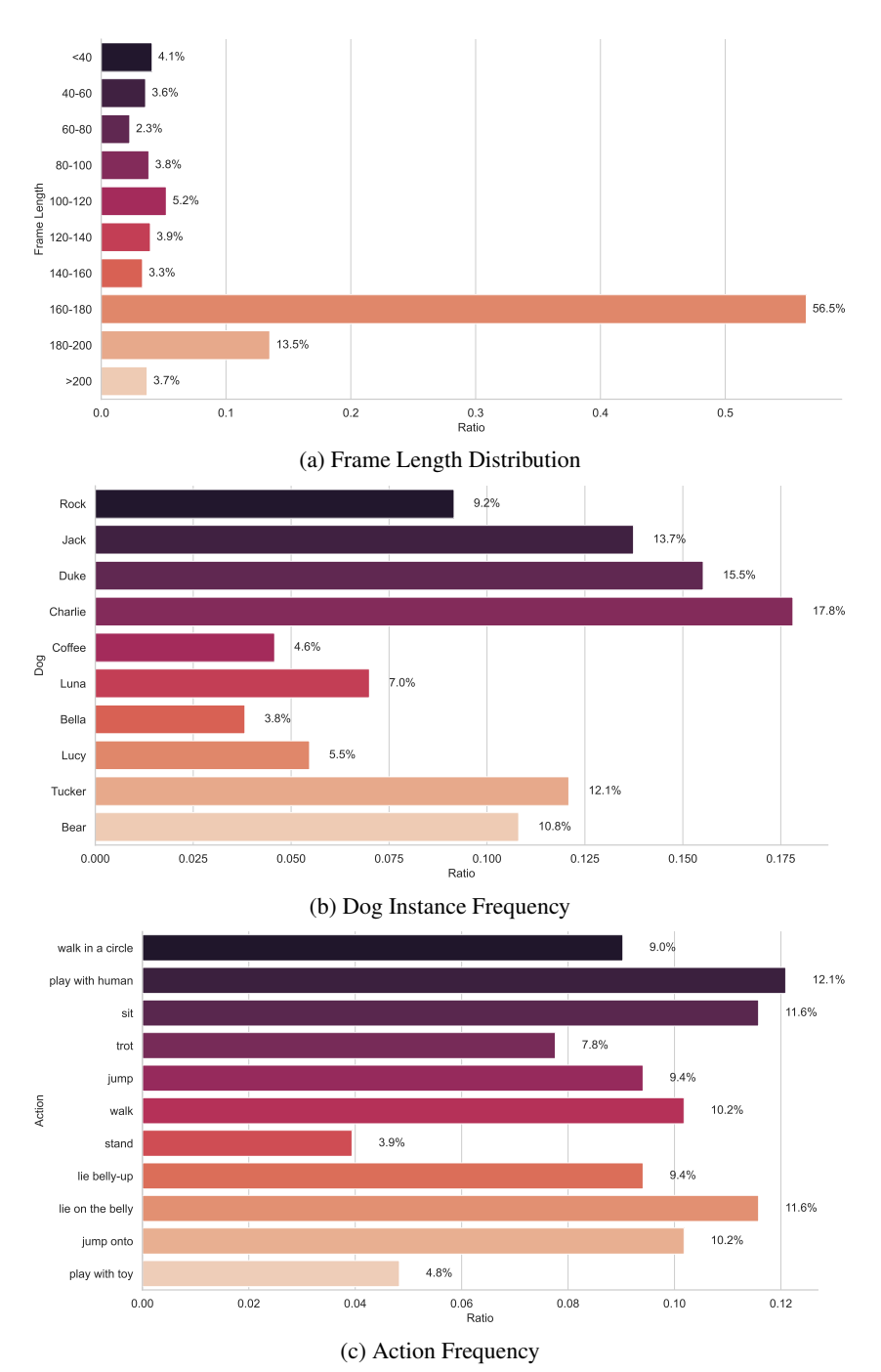


Figure A1: Statistics of *DogMo*. Notably, the action "stand" denotes the dog standing upright on its hind legs.

Foot Skating Foot skating measures the unintended horizontal displacement of the feet while in contact with the ground, indicating unrealistic gait motion. The metric is calculated by averaging the horizontal velocity of the feet whenever their distance to the ground plane is below 0.04m.

# **B** Dataset Statistics

**Statistics** We provide additional statistics for the *DogMo* dataset in Fig. A1. Figure A1a illustrates the distribution of motion sequence lengths. In *DogMo*, frame counts range from 13 to 286, with over half of the sequences falling between 180 and 200 frames. The average frame length is approximately 155. Figure A1b presents the distribution of motion data across 10 individual dog instances in *DogMo*.

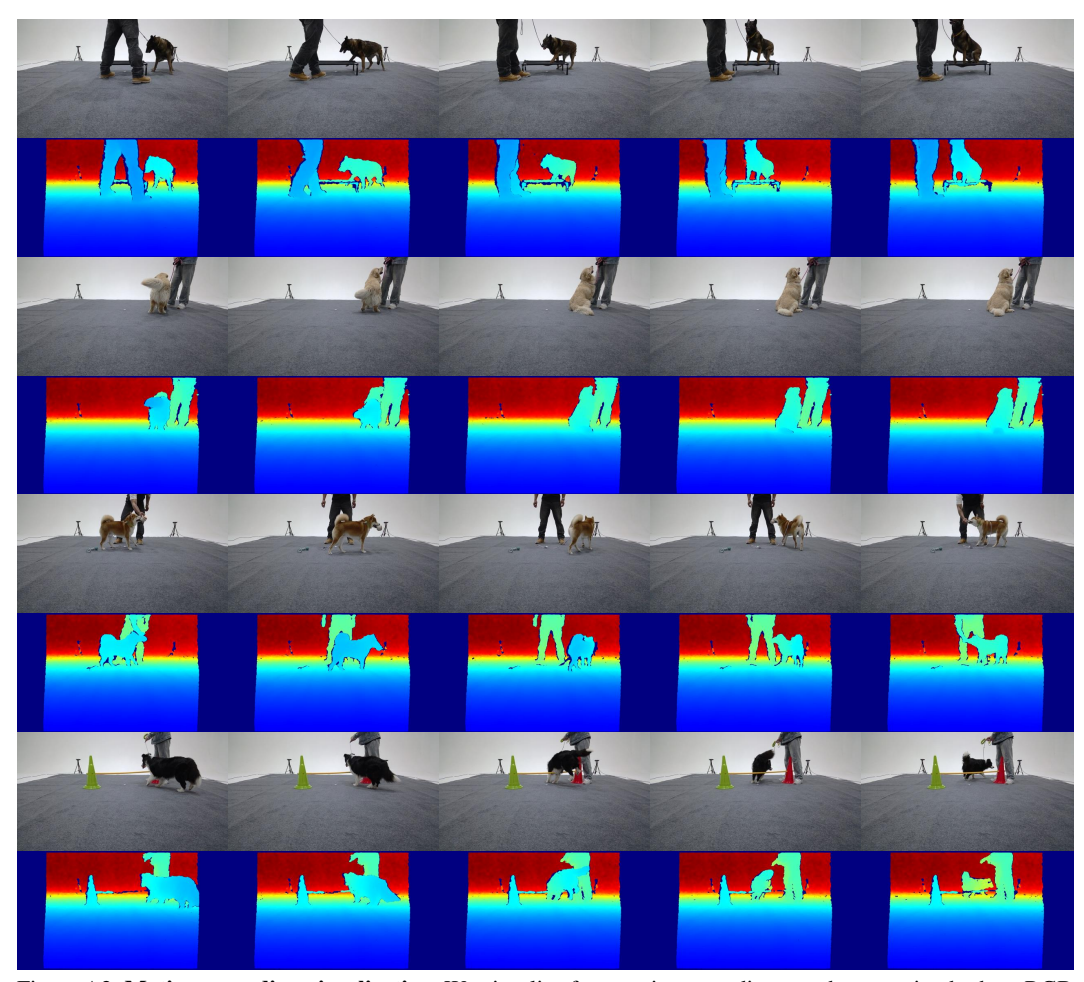


Figure A2: **Motion recording visualization.** We visualize four motion recordings, each presenting both an RGB sequence and a depth sequence.

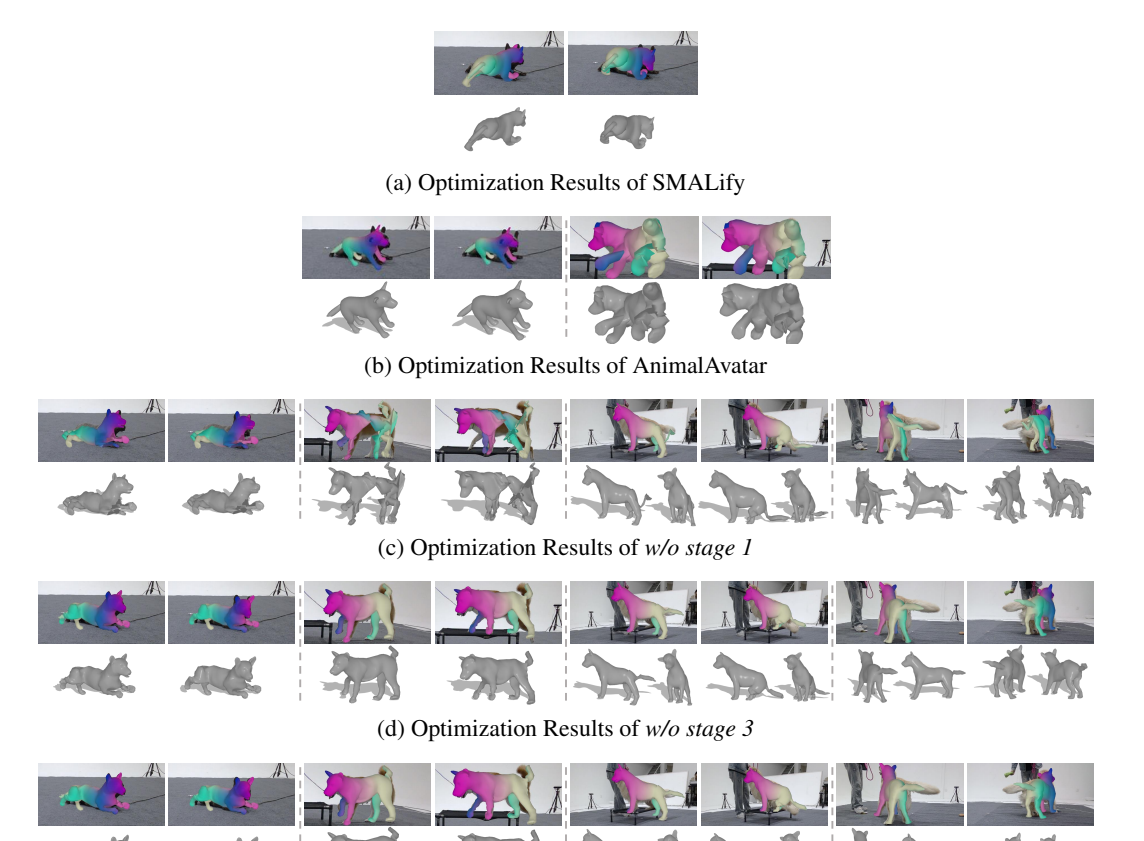
Some dogs, *e.g.*, Charlie, appear more responsive to the trainers, so we collect more motion sequences from those instances. Additionally, each motion sequence in **DogMo** is annotated with one of 11 predefined action categories. The motion distribution over these action types is shown in Fig. A1c.

**Visualization of Motion Recordings** We additionally provide visualizations of the motion recordings in Fig. A2. For video demonstrations, please refer to the supplementary demo video.

# C Additional Results

**Qualitative Result Comparison** In Fig. A3, we compare the qualitative results of the baseline models with those of our full model. When recovering dog motion from a single-view RGB image, the comparison shows that both SMALify [Biggs et al., 2020] and AnimalAvatar [Sabathier et al., 2024] fail to capture the dynamics of body parts, particularly the leg movements, resulting primarily in global translation and orientation changes. Without the initialization provided by the first stage, the method struggles to reconstruct the complete motion. We also provide video demonstrations in the supplementary demo video.

**Failure Cases** We present several failure cases produced by our method in Fig. A4. As shown in the results, when the dog is curled up in a resting position, it becomes difficult to distinguish individual body parts due to the uniform texture across the body, leading to inaccurate reconstruction. Additionally, when the dog is occluded by the dog trainer, particularly the distinguishable body parts such as the head, the limited visual information also leads to poor reconstruction of the body shape.



(e) Optimization Results of Our Full Method

Figure A3: **Qualitative result comparison.** (a) For the optimization results of SMALify, we present motion recovery from single-view RGB images. (b) For the optimization results of AnimalAvatar, we present motion recovery from single-view RGB images and single-view RGB-D images. (c) (d) For the other baseline methods, we show results under four settings, *i.e.*, single-view RGB, single-view RGB-D, multi-view RGB, and multi-view RGB-D, arranged from left to right. For each setting, we show two frames from the motion sequence.

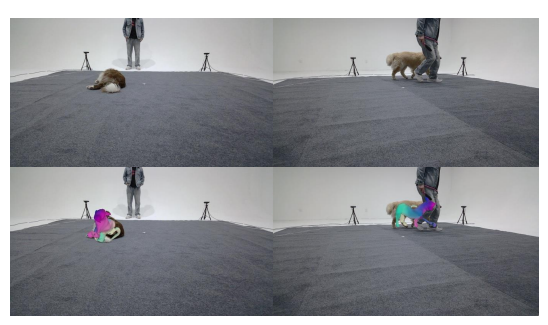


Figure A4: Failure cases.

# **D** Additional Experiments

Impact of Different Initial s in w/o stage 1 As shown in Tab. A1, the model w/o stage 1 exhibits large variations in Pene% and Foot Skating under different scaling factors s. When s=0.3, the model tends to retain a smaller body size, causing the mesh to float above the floor. This leads to reduced penetration and fewer contacts, and non-contact meshes inherently yield zero penetration and zero foot skating. Conversely, when s=1.0, the resulting meshes penetrate deeply into the floor, producing a higher penetration ratio. Excessive penetration also reduces the number of valid contact frames for foot skating computation, thereby lowering the averaged foot skating score. Both variants show low Jitter. We speculate that without stage 1 optimization, the pipeline primarily adjusts global

Table A1: Impact of different initial s in w/o stage 1.

Method	Single-view RGB						
	Pene <sub>%</sub> ↓	Jitter↓	FS ↓				
w/o stage 1 ( $s = 0.3$ ) w/o stage 1 ( $s = 1.0$ )	0.0796	$0.0056 \\ 0.0096$	0.0019 0.0147				

Table A2: Quantitative results with simpler temporal smoothing alternatives.

Setting	Method	IoU↑	IoU <sub>w5</sub> ↑	F-score ↑	Jitter ↓
Single-view RGB	Kalma Spline	$0.6251 \\ 0.4821$	$0.5015 \\ 0.2968$	$0.3119 \\ 0.3426$	$0.0211 \\ 0.0047$
	Ours	0.6505	0.5247	0.3593	0.0249
Single-view RGB-D	Kalman Spline Ours	0.6248 $0.4812$ $0.6414$	0.4945 $0.3031$ $0.5228$	0.6889 $0.6951$ $0.7673$	0.0178 $0.0037$ $0.0162$
Multi minu DCD					
Multi-view RGB	Kalman Spline Ours	0.6021 $0.4769$ $0.6258$	$0.3937 \\ 0.2379 \\ 0.4490$	0.8586 $0.8080$ $0.9107$	0.0165 $0.0036$ $0.0142$
Multi-view RGB-D	Kalman Spline Ours	0.5907 $0.4748$ $0.6286$	0.3847 $0.2337$ $0.4549$	0.8595 $0.8089$ $0.9137$	0.0159 $0.0045$ $0.0143$

translation and orientation in the second stage while neglecting high-frequency motion details. As a result, most joints move more smoothly with reduced dynamics, leading to lower jitter values.

**Simpler Temporal Smoothing Alternatives** We replace the smoothness optimization with simpler Kalman and spline smoothing in the third stage, which yields smoother results with reduced jitter. However, they also result in slightly lower IoU and F-score. The results are presented in Tab. A2.

## E IRB (Institutional Review Board)

This study does not involve human subjects or physiological experiments. The dataset in this work is collected from videos of dogs in natural environments without invasive procedures or interventions. According to our institution's research ethics policy, IRB (Institutional Review Board) approval is only required for studies involving human participants or biological experimentation. Therefore, no IRB approval is necessary or applicable for this research.

# F Broader Impact

This work focuses on reconstructing the motion of dogs from visual data, contributing to the broader understanding of animal motion in computer vision and machine learning. Potential positive societal impacts include enabling improved animal behavior analysis and advancing animation or simulation technologies for education, film, and virtual environments. Additionally, the data and techniques may support future research in biologically inspired locomotion in robotics. Given the nature of the work, we do not anticipate any significant negative societal impacts.